ACS Photonics

Letter

pubs.acs.org/journal/apchd5

Bright Multicolored Photoluminescence of Hybrid Graphene/Silicon Optoelectronics

Ken Liu,*[,†] Zhi Hong Zhu,[†] Xiu Jian Li,[‡] Jian Fa Zhang,[†] Xiao Dong Yuan,[†,§] Chu Cai Guo,[†] Wei Xu,[†] and Shi Qiao Qin[†,§]

[†]College of Optoelectronic Science and Engineering, [‡]College of Science, and [§]State Key Laboratory of High Performance Computing, National University of Defense Technology, Changsha, Hunan 410073, China

Supporting Information

ABSTRACT: Graphene does not possess a band gap, and hot carrier relaxation in graphene is an ultrafast processs. This leads to a very low emission efficiency of graphene. We demonstrate bright multicolored frequency-upconverted photoluminescence from graphene via three-photon absorption by femtosecond laser injection at a communication wavelength 1.57 μm. The broadband and multiwavelength emission from graphene is based on the model of ultrafast electron−hole pair recombination and asymmetrical energized electron−hole radiation recombination in graphene. Furthermore, we show photoluminescence variation with blue light emission in the graphene/silicon hybrid system, with 2−3 orders of emission efficiency increase. The results demonstrate hot carrier multiplication and hot carrier scattering in graphene and could help to study the population inversion and broadband lasing of graphene.

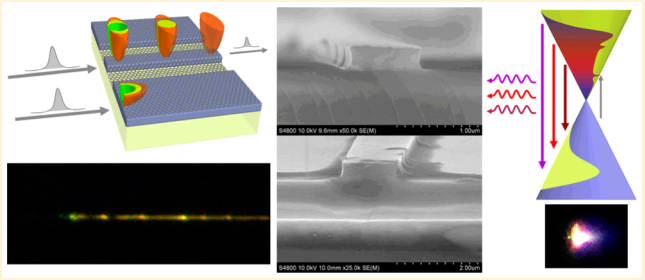

KEYWORDS: *graphene, silicon, frequency-upconverted photoluminescence, broadband, hot carrier multiplication, hot carrier scattering*

Graphene is a monolayer material that exhibits unique electrical and optical properties. For example, it has carriers with zero effective mass and exhibits a broadband linear absorbance of 2.3%, which is defined by the fine structure constant,[1] and electrons and holes of graphene have a symmetrical linear energy−momentum dispersion relationship.[2−4] Integrating graphene to a silicon waveguide with complementary metal−oxide semiconductor (CMOS) technology can enhance light absorption with planar propagation. This ability has been utilized to achieve CMOS-compatible broadband electroabsorption modulators[5] or photodetectors.[6−8] The lack of band gap makes graphene seem difficult for light generation. Recent studies show that graphene has third-order nonlinear susceptibility 4−5 orders larger than that of silicon.[9,10] However, visible third-harmonic generation (THG) and photoluminescence in graphene are still difficult to achieve. The first reason is that graphene has no band gap and the Fermi level of pristine graphene is zero, which makes graphene a highly absorptive material. The second reason is that the light−matter interaction length is very short at normal or oblique incidence[11,12] since monolayer graphene has a thickness of only 0.34 nm. The third reason is that the photoexcited nonequilibrium carriers relax rapidly with carrier−carrier and carrier−phonon interactions to thermal equilibrium.[13] Even with intense optical injection, the signals of THG and photoluminescence are very weak, and highly sensitive photomultiplier tubes[12,14] or an avalanche photodiode[15] is needed to detect the emission signals.

RESULTS AND DISCUSSION

To overcome these limitations, heavily n-type chemically doped graphene (see Experimental Section) is used in our experiment, since the absorption of graphene can be controlled by tuning the Fermi level with electrostatic doping[5] or chemical doping.[10] The graphene sample is layered on a silicon waveguide in order to enhance light−graphene interactions by coupling the injection pulse to the silicon waveguide.[5,10] With planar injection by a compact 1.57 μm mode-locked fiber laser (MLL), we found that the ultrafast intense photodoping greatly changed the carrier scattering and relaxation process of graphene. We demonstrate bright multicolored photoluminescence of graphene, which is different from previous reports.[14−18] The emission efficiency is several orders greater than the previous report,[16] and the emitted light with different colors can be clearly observed by the naked eye from a microscope.

Light emission of graphene is schematically illustrated in Figure 1a. The graphene sample was clad on 0.26 μm thick silicon on an insulator (SOI), where silicon waveguides are etched with widths ranging from 0.60 to 2.0 μm to ensure the wave propagation with wavelength to 2.4 μm. Graphene was also clad on silicon ridge waveguides with a slot structure on 1.5 μm thick SOI to study the photoluminescence at different

Received: February 5, 2015
Published: June 16, 2015

DOI: 10.1021/acsphotonics.5b00051
ACS Photonics 2015, 2, 797−804

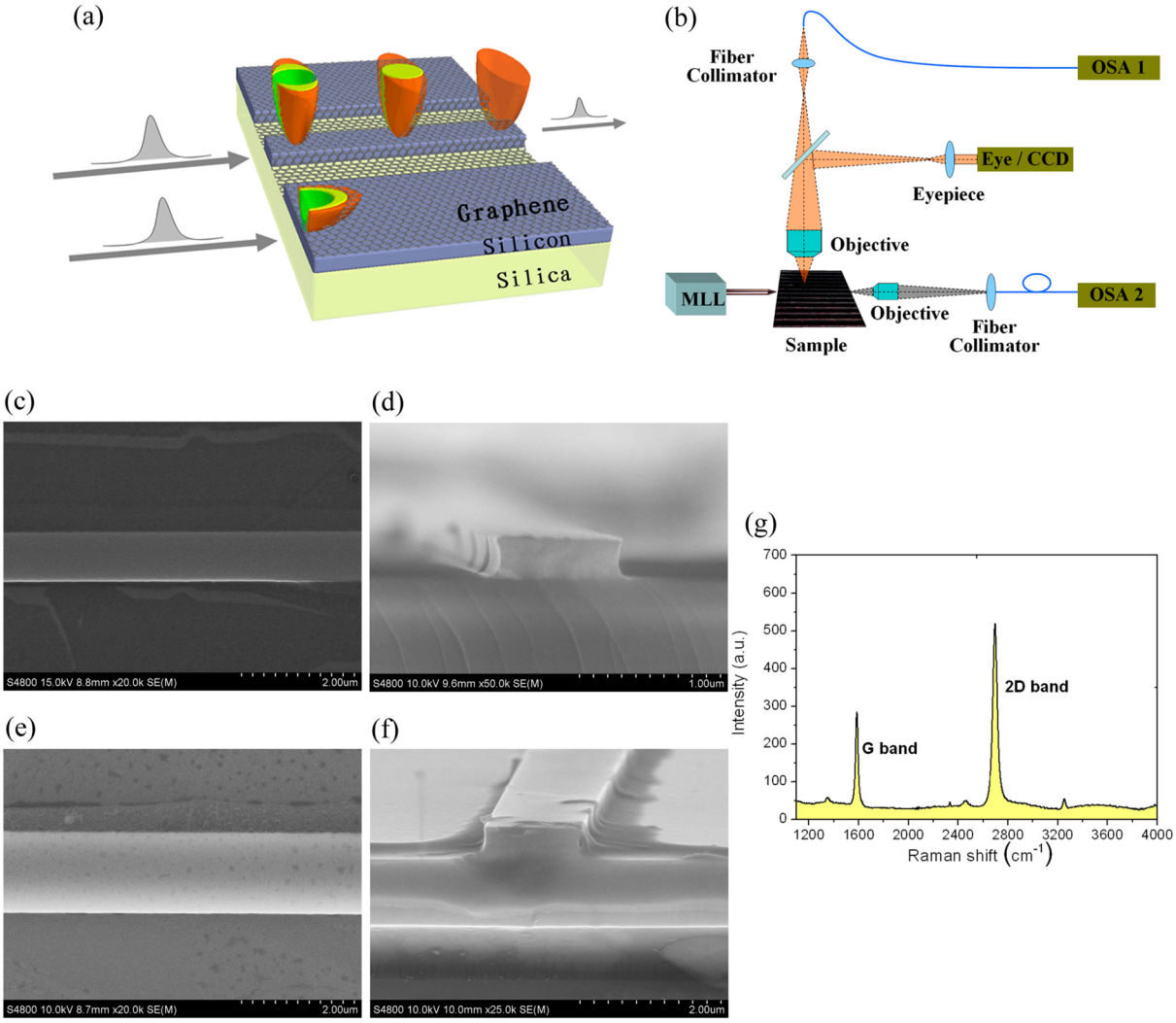

Figure 1. Photoluminescence emission from graphene. (a) Three-dimensional schematic of the sample: monolayer graphene is on top of a silicon slab and waveguide. Ultrafast pulses are coupled into the structure. (b) Schematic of experimental measurement setup. SEM image of (c) top view and (d) cross section view of a graphene/silicon strip waveguide. The thickness of the silicon layer is 0.26 μm. SEM image of the (e) top view and (f) cross section of a graphene/silicon ridge waveguide. The thickness of the silicon layer is 1.5 μm, and the etched thickness is 0.4 μm. (g) Raman spectra of the graphene sample on silicon.

conditions (see Experimental Section). A femtosecond laser was coupled into a silicon waveguide or the slab by a tapered optical fiber. Emitted light was collected vertically to an optical spectrum analyzer (OSA 1), and transmitted light was collected horizontally to OSA 2 (Figure 1b) to record the transmission in the waveguides. Scanning electron micrograph (SEM) views of the graphene on the silicon waveguide are shown in Figure 1c–f. Figure 1g shows the Raman spectrum of the chemically doped graphene, which identifies the single layer of graphene. By comparing our graphene sample with the reference,[19] we estimate that the doping density is 3.7×10^{13} cm^{-2} and Fermi level is 0.71 eV (see Supporting Information S1).

Figure 2 shows the charge-coupled-device (CCD) camera image of visible light emission through a microscope when femtosecond pulses at a communication wavelength of 1.57 μm are incident and coupled into the graphene/silicon slab (see the Experimental Section for parameters of the femtosecond laser). The images (Figure 2) and emission spectra (Figure 3a–c) show that the emissions are broadband. For a continuous light wave injection with an input power of 1 W, no emission can be detected (Figure 3c, dark yellow dot–dashed line), while for a femtosecond laser injection (the energy is estimated as 10 pJ with a duration of 130 fs) there is no emission for the silicon waveguide if there is no graphene on it (Figure 3b, dark yellow dot–dashed line) (see Supporting Information S3 for the details of silicon photoluminescence). From Figure 2d, we can find that the emission comes from the area where graphene exists. It should be noticed that there is a nanoparticle on the surface of the waveguide at the right side, and no light emission is observed there. Thus, we can show that the emission is from the graphene and not from the silicon or the scattering introduced by the graphene or particle on the waveguide. Since the output power of the femtosecond laser cannot be changed, we use different waveguides and coupling efficiencies (see the Experimental Section) to observe the emission dependence on the input power. With the increase of injection energy, there are always three emission peaks, at about 545, 680, and 900 nm, respectively. At the same time, the intensities of the two peaks at the short wavelengths increase and the positions of the emission peaks almost do not change (Figure 3a–c). In order to distinguish the emission with nonlinear processes, such as four-wave mixing and stimulated Raman scattering, we

DOI: 10.1021/acsphotonics.5b00051
ACS Photonics 2015, 2, 797–804

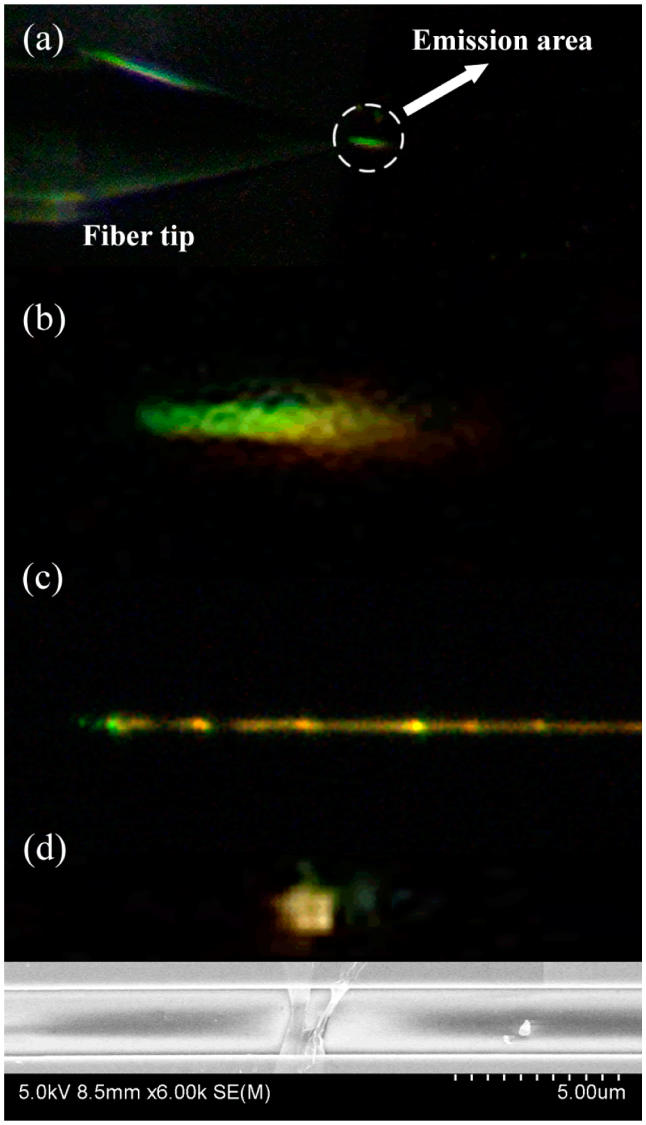

Figure 2. Photoluminescence emission imaged by a CCD camera. (a) Femtosecond pulse is coupled to the graphene/silicon slab, with weak microscope lamp illumination on a fiber tip and the sample surface. (b) Magnified image of the emission area without microscope lamp illumination. (c) Pulse is coupled to a silicon waveguide fully covered with graphene and (d) partially covered with graphene. Bottom in (d) is the SEM image of the silicon waveguide with only one part covered with graphene.

measured the transmission spectra from the slab and waveguide (Figure 3d). No Stokes waves, anti-Stokes waves, or four-wave mixing was detected by OSA 2 in the range 1.2 to 2.4 μm. Therefore, we can conclude that the yellow and red light generation is not a nonlinear optical process but photoluminescence of the recombination of optically exited carriers.

Since the silicon layer has a higher refraction index than the insulator layer, it forms a Fabry−Perot cavity. The photoluminescence emissions thus have interference effects and oscillations. This can be proved since there are two kinds of silicon substrates with different thicknesses, 0.26 and 1.5 μm, respectively, and the numerical simulations of different substrates (Figure 3a−c) agree well with the measured data in these two cases (see detail in Supporting Information S2).

One-photon absorption, although prohibited due to the Paul blockade, exists because of defects of graphene. However, the emission spectra are obviously different from the thermal emission spectrum of graphene[16] caused by one-photon absorption. It is also different from doped graphene with sharp emission peaks at the Fermi level.[17] Although three-photon absorption is a higher order nonlinear process, it is not always weaker than two-photon absorption (e.g., Zheng' work[20]). The sharp increase of the emission from about 510 nm, the first emission peak at about 545 nm, and the second emission peak at 680 nm (Figure 3a−c) show that the photoluminescence is caused by three-photon absorption (a five-order nonlinear process) rather than two-photon absorption (a three-order nonlinear process), because two-photon absorption (at about 785 nm) cannot induce photoluminescence emission at such short wavelengths.

The mechanism of the photoluminescence can be illustrated in Figure 4. After the three-photon absorption, photoexcited electrons and holes with the same momentum appear simultaneously in the conduction and valence band (Figure 4a). The hot carrier relaxation of graphene has a short lifetime (~170 fs) and longer lifetime (>1 ps) measured by other groups.[13,21] Increase of the ratio of the recombination rate to the hot carrier relaxation rate can lead to the increase of emission efficiency[22] and enable effective radiative recombination during hot carrier relaxation to thermal equilibrium (Figure 4b).

The recombination or spontaneous emission rate R_{sp}^{21} can be written as[23] (see details in Supporting Information S4)

$$R_{sp}^{21}(E_{21}) \propto R_r f_2^n(E_{21}) f_1^p(E_{21}) \tag{1}$$

where R_r is the radiative transition rate, f_2^n and f_1^p are the electron and hole occupation probabilities of the density of states (DOS) of graphene, $f_2^n = n_{ph}(E_2)/\rho(E_2)$, and $f_1^p = p_{ph}(E_1)/\rho(E_1)$.

The variation of photoexcited electron and hole densities $n_{ph}(E_2)$ and $p_{ph}(E_1)$ at energy levels E_2 and E_1 can be written as

$$\frac{dn_{ph}(E_2)}{d(-E_{21})} = -\gamma(E_2) R_{sp}^{21}(E_{21}) - \Gamma(E_2)\, n_{ph}(E_2) \tag{2}$$

$$\frac{dp_{ph}(E_1)}{dE_{21}} = -\gamma(E_1)\, R_{sp}^{21}(E_{21}) - \Gamma(E_1)\, p_{ph}(E_1) \tag{3}$$

where γ is the recombination coefficient and Γ is the scattering coefficient.

During hot carrier relaxation and recombination, $n_{ph}(E_2)$ and $p_{ph}(E_1)$ decrease with the decrease of E_{21}, which means that relaxation and recombination deplete hot carriers. As $n_{ph}(E_2)$ and $p_{ph}(E_1)$ decrease sharply, $R_{sp}^{21}(E_{21})$ decreases. Thus, there should be one emission peak below the three-photon absorption energy level (peak A in Figure 3a−c), and the emission power decreases quickly as the wavelength increases. It should be noted that $R_r \propto (|\vec{E}|^2/\omega_{21}^2)\cdot\rho_r(\hbar\omega_{21})$, and f_2^n and $f_1^p \propto 1/\omega_{21}$, where $\vec{E}$ is the electrical field and ρ_r is the DOS of electron−hole pairs. Thus, from eq 1, it can be deduced that R_{sp}^{21} increases with the decrease of ω_{21}. This is especially helpful for terahertz radiation in a pristine graphene, since at the terahertz range, R_{sp}^{21} is much higher than that at visible and infrared frequencies. In theoretical simulations, we assumed that hot electrons are centered at the energy level of about 1.18 eV and hot holes at the energy level of about −1.18 eV with Gaussian-like shapes in energy space after three-photon absorption, and the theoretical emission spectra can be

DOI: 10.1021/acsphotonics.5b00051
ACS Photonics 2015, 2, 797−804

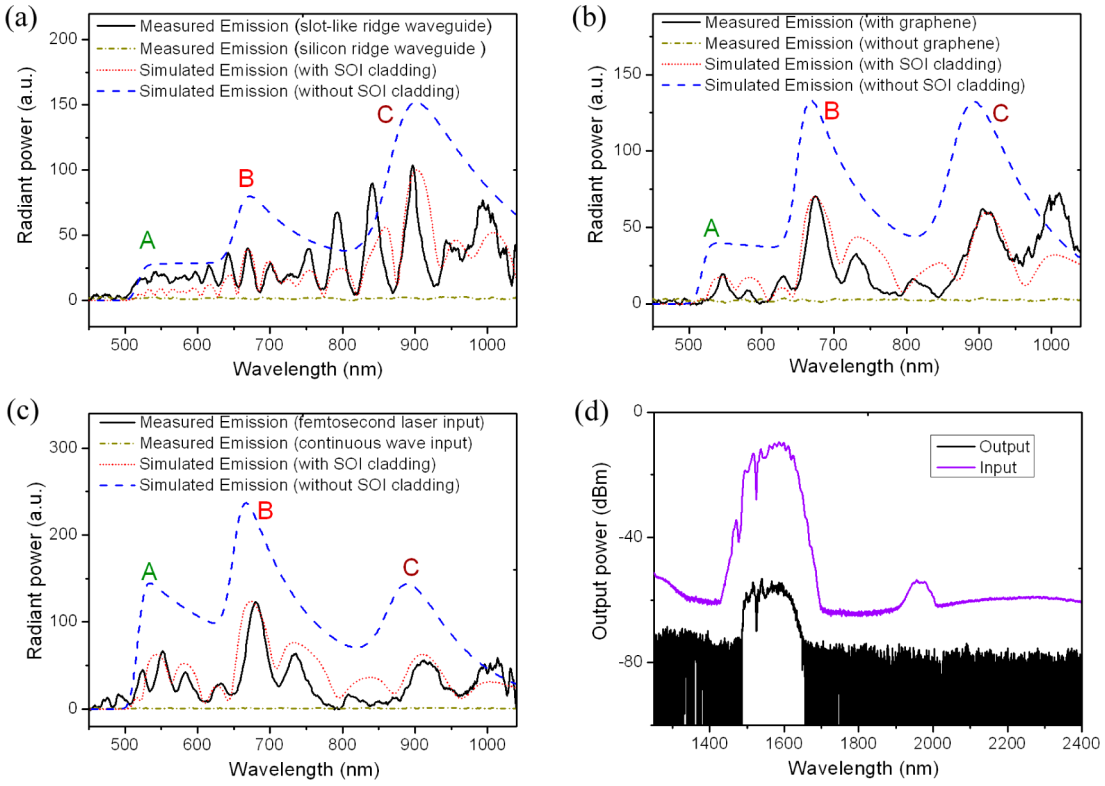

Figure 3. Photoluminescence and transmission spectra of graphene. (a) Photoluminescence spectra collected from graphene that is embedded in a slot-like silicon ridge waveguide (black line) (the structure is shown in Figure 1e and f) and directly from the silicon ridge waveguide (without graphene on it) (dark yellow dot−dashed line). The blue dashed line is the simulated graphene emission spectrum, while the red dotted line is the simulated emission spectrum with SOI cladding. The integration time is 50 s. (b) Photoluminescence of graphene on a silicon waveguide (black line) (the structure is shown in Figure 1c and d) and pure silicon waveguide without graphene on it (dark yellow dot−dashed line). The integration time is 10 s. (c) Photoluminescence of graphene on a silicon waveguide (the structure is shown in Figure 1c and d) with an increased injection power (black line). Emission for a continuous wave injection (dark yellow dot−dashed line). In theoretical simulations, the injection power shown in (b) is 2 times and in (c) is 4 times greater than that shown in (a). (d) Measured injection (purple line) and transmission spectrum (black) from the graphene/silicon waveguide (the structure is shown in Figure 1c and d). Length of the graphene/silicon waveguide is about 0.1 mm.

obtained from the equations discussed above. From the calculation (see Supporting Information S4), we can always find that the emission decreases quickly following the emission peaks, since the radiation recombination depletes the hot carriers quickly. Another emission peak is near the Fermi level (peak C in Figure 3a−c). This is because the radiation recombination rate increases with the great increase of the electron density near the Fermi level.

During hot carrier relaxation to thermal equilibrium, there is a huge amount of phonon emission followed by carrier-phonon scattering. The existence of a huge amount of phonons in graphene during the ultrafast relaxation process would cause an uncertainty in electronic structure in the $(\omega, \vec{k})$ space,[24] which means that the states are not located at $(|\vec{k}|, \hbar v_F|\vec{k}|)$ rigorously. The DOS ρ of electrons or holes cannot be considered as a function of energy $\rho(\hbar\omega)$ or momentum $\rho(\hbar|\vec{k}|)$ any more.[24] It is a function of both energy and momentum, $\rho(\hbar\omega, \hbar\vec{k})$. Thus, electron−hole pairs with the same $\vec{k}$ could have asymmetric energies, i.e., electrons at the Fermi level E_F and holes at the energy level $E_{TPA} = -(3/2)\hbar\omega_0$ (Figure 4c). Hence, in the ultrafast process, photons can emit from radiative recombination of asymmetrically energized electron−hole pairs (AEEHP). This causes another peak (peak B) in the emission spectra (Figure 3a−c). It should be noticed that this process is different from the phonon-assisted hot luminescence of silicon discussed in the literature.[22] The recombination here is a direct recombination, without participation of phonons. The coupling between phonons and electrons or holes only helps to expand the electronic structure of graphene. That is to say, the electronic structure of graphene changes first, and efficient electron−hole recombination happens after the electronic structure change.

As shown in Figure 3, peak A increases with the increase of excitation power. This is consistent with the image shown in Figure 2b. In Figure 2b, the femtosecond laser is coupled to the graphene/silicon slab, and thus the excited light is not confined by the waveguide and decreases with propagation. The spatially distributed color image from Figure 2b corresponds to the change from peak A (Figure 3c) to peak B (Figure 3a). Peak C is not revealed clearly in Figure 2b because the CCD camera has a low response at the near-infrared range.

After photon excitation, carrier multiplication is an interesting effect that may happen in graphene in the ultrafast process.[25,26] Carrier multiplication including impact ionization and Auger heating, which are both Auger processes,[23] may play an important role in the relaxation of photoexcited carriers in graphene. Carrier multiplication has been predicted in some studies with pristine graphene without consideration of radiative recombination,[21] and it is believed that carrier multiplication plays a key role in hot carrier relaxation from the experiment. However, in direct measurements,[27] evidence

DOI: 10.1021/acsphotonics.5b00051
ACS Photonics 2015, 2, 797−804

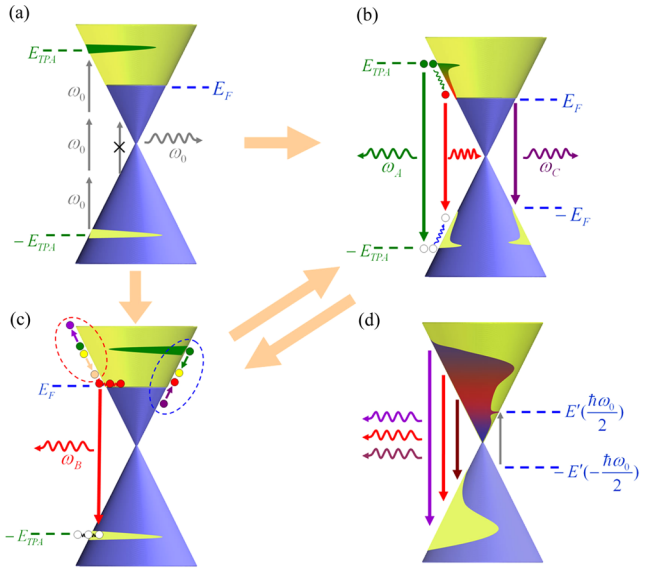

Figure 4. Ultrafast nonequilibrium radiation recombination process in graphene. (a) The Fermi level E_F is higher than $\hbar\omega_0/2$ and lower than $3\hbar\omega_0/2$. Graphene is transparent for the injected photons with energy $\hbar\omega_0$ but absorptive for the photons with energy $3\hbar\omega_0$. Photoexcited electrons are populated at energy $3\hbar\omega_0/2$ after femtosecond pulse excitation. (b) Electron–hole recombination during their energy exchange with phonons to thermal equilibrium. Holes in the valence band would be consumed out near $-E_F$ with the sharp increase of electron density at E_F. (c) AEEHP radiative recombination, hot carrier multiplication (blue dashed circle), and hot carrier scattering (red dashed circle) in graphene. During the ultrafast nonthermal equilibrium process, the sudden increase of phonon densities induces the electron–hole occupation broadening in $(\omega, \vec{k})$ space, and thus direct electron–hole recombination occurs with electron–hole pairs at asymmetric energy levels. In the hot carrier multiplication process, the net effect is that one hot electron above the Fermi level exchanges its energy and momentum with another electron below the Fermi level and leads to an increase in the number of hot electrons above the Fermi level. In the hot carrier scattering process, two hot electrons above the Fermi level exchange their energy and momentum, and the number of hot electrons above the Fermi level do not change. (d) Electron–hole pair recombination process with intense laser excitation. AEEHP radiative recombination, hot carrier multiplication, and hot carrier scattering play key roles for broadband radiation and radiation frequency blue shift.

of carrier multiplication cannot be found. Another study still shows that strong Auger scattering can affect the Landau levels in graphene.[28] It should be difficult to use intrinsic graphene to observe linear carrier scattering in the visible range. Because in intrinsic graphene the energy of electrons in thermal equilibrium is below the Dirac point, it is difficult to use hot carriers to collide these electrons to the energy level corresponding to visible frequency.

Since the graphene used in this paper is n-doped graphene and the Fermi level is above zero, we use the photoluminescence spectra during the ultrafast process to study hot carrier multiplication and hot carrier scattering in graphene. Hot carrier multiplication is seldom studied,[29] and the concept is different from carrier multiplication (see Supporting Information S5 for a detailed description). However, they both reveal the linear carrier collision mechanism in graphene. From the emission spectra (Figure 3a–c), we cannot find the existence of hot carrier multiplication and scattering. This, however, does not mean that these effects never exist in graphene. They can be considered as a weak perturbation of the electron density in this case, as shown in Figure 4c, and thus have little effect on the emission spectra. This is consistent with theoretical predictions (see Supporting Information S4), because in the theoretical simulations the density of photoexcited hot electrons is assumed to be lower compared to the density of electrons in the thermal equilibrium state below the Fermi energy level. Thus, we think that decreasing the sizes of the graphene to micrometer-scale would reduce the numbers of electrons and increase the density ratio between hot carrier multiplication induced high energy electrons and electrons at the thermal equilibrium state. This is because electrons in micrometer-size graphene at high energy states cannot exchange energies and momentum with other electrons outside this micrometer area in real space. Also, in energy space, the decrease of graphene size would reduce the states of graphene. Electrons in the valence band would be pumped efficiently to the conduction band via three-photon absorption, sharing their energy and momentum with the electrons below the Fermi level, pumping these electrons to higher levels, and leaving holes far below the Fermi energy in the conduction band. However, electrons at the energy $\hbar\omega_0/2$ in the conduction band can be collided to higher energy states, but holes cannot be left here, since electrons at the energy level $-(\hbar\omega_0/2)$ would be pumped to the energy level $\hbar\omega_0/2$ via absorbing one photon with the energy $\hbar\omega_0$, and there should be a peak in the electron density distribution at the energy level around $\hbar\omega_0/2$ (Figure 4d).

We achieved microsized graphene by simply using the fiber tip to break the graphene/silicon sample boundary. Graphene was then broken into microsized pieces at the SOI boundary. If the graphene/silicon pieces are still on the SOI slab, there is no photoluminescence of silicon since there are not enough surface states, but the graphene emission spectra (Figure 5, blue line) change compared with the spectra shown in Figure 3. The

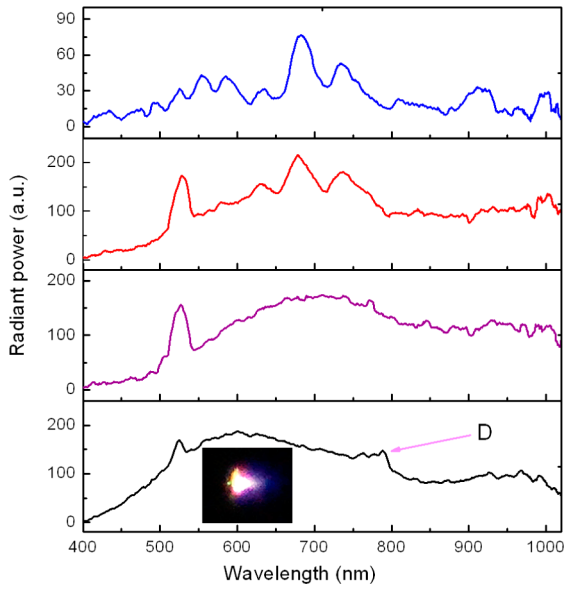

Figure 5. Photoluminescence radiant power variation of a graphene/silicon micropiece. The integration time is 20 s (blue, red, and purple lines) and 5 s (black line), respectively. Emission peaks at 523 nm are THG in silicon. Inset is blue light emission capatured by the CCD camera, and the small green spot in the inset is the THG emission area.

DOI: 10.1021/acsphotonics.5b00051
ACS Photonics 2015, 2, 797–804

main difference is the increase of the emission power following peak A (at about 540 nm) and the decrease of the emission power ratio near the Fermi level (at about 870 nm). This demonstrates the hot carrier multiplication in graphene so that more electrons are populated following peak A and indicates that the hot carrier multiplication induced electron density is comparable with the density near and below the Fermi level. By increasing the coupling efficiency, the hot carrier multiplication process becomes more and more obvious from the spectra (Figure 5, red line).

If the graphene/silicon piece is off the SOI slab, photoluminescence of graphene can be exited (Figure 5, purple and black lines). The emission is not from a silicon nanocrystal, since the silicon photoluminescence has different emission spectra (see Supporting Information S3 for silicon photoluminescence spectra). If we move the sample to a few micrometers away, the emission spectra are similar (see Supporting Information S6). Comparing the two spectra (Figure 5, red and purple lines), it can be deduced that the emission is from graphene. After increasing coupling efficiency, the emission peak shifts from 680 nm to 600 nm and an emission peak appears at around 789 nm (see Supporting Information S6). We think that the peak is not from second-harmonic generation (SHG) since the SHG peak should be located at 785 nm with a narrow band. The emergence of the emission peak should be from AEEHP radiative recombination of electrons at the energy level $\hbar\omega_0/2$ and holes at $-(3\hbar\omega_0/2)$, as predicted from Figure 4d. The peak at about 789 nm proves that no phonon participates in the recombination since with participation of phonons the wavelength change should be much greater than 4 nm. The change of emission peak from 680 nm to 600 nm proves the hot carrier multiplication effect in graphene as more electrons were populated above the Fermi energy. Another proof of the hot carrier multiplication effect is the increase of photon emission with energy less than $2E_F$, which means that the number of holes above $-E_F$ is increased and shows the slow variation of the number of electrons around E_F. The emission area (Figure 5, black line) is less than 10% of the whole graphene (Figure 2); thus we estimate that emission efficiency has been increased by 2−3 orders compared with the emission spectra shown in Figure 3, and the emission efficiency is greater than 5×10^{-5} (Supporting Information S7).

Hot carrier scattering also becomes obvious together with hot carrier multiplication. One hot electron in the graphene can transfer its energy to another hot electron which is at a high energy level above the Fermi level, and the latter is collided to an even higher energy level (Figure 4c). This could cause the blue shift of the emission spectrum with the latter hot electron−hole recombination. The effect of these recombination processes can be enhanced with the increase of hot electron density, and the schematic is shown in Figure 4d. Blue light emission can be directly observed from the inset image and emission spectrum shown in Figure 5 (black line). However, the blue shift stops at a wavelength shorter than about 410 nm in this case, as with the increase of energy, the energy-momentum dispersion of graphene deviates more and more from a linear relationship and the hot carrier scattering effect becomes more and more difficult.

For a broken graphene, as shown in Figure 2d, or a bent graphene with large curved angles, there are boundary states at the graphene boundaries. These boundary states can be considered as defect states and would greatly affect the photoluminescence. However, the mechanism is not clear now, and the boundary effect on the photoluminescence needs further study.

In conclusion, we investigate the properties of photoexcited carriers in the monolayer graphene/silicon hybrid system at room temperature and demonstrate the ultrafast light emission mechanism. Photoluminescence measurement is a powerful and convenient method that can be used to study graphene. The photoluminescence spectra can also be used to study electronic properties of graphene, such as detecting the Fermi level (Figure 3) other than from Raman spectra.[19,30] It should be noted that there is no resonant structures in our samples, which means that the radiation efficiency may be greatly enhanced with optical confinement (i.e., high quality factor cavities). The AEEHP radiative recombination provides a new way of nonlinear frequency generation without nonlinear frequency conversion such as optical parametric oscillations. The results show that ultrafast photoluminescence could be a very efficient way for light emission of materials without a band gap, and with the increase of emission efficiency, hot carrier multiplication and hot carrier scattering effects would play important roles in the recombination and relaxation. Thus, we can expect broadband supercontinuous stimulated emission of graphene in both the visible and infrared region in the future.

EXPERIMENTAL SECTION

Silicon waveguides were fabricated from a 0.26 μm thick silicon on a 2.0 μm thick insulator wafer. The width of the waveguides varies from about 0.6 to 2.0 μm to ensure the support of wave propagation with a wavelength ranging from 1.2 to 2.4 μm. The waveguides were fabricated by e-beam lithography (Crestec CABL 4000) with C4-type poly(methyl methacrylate) (PMMA) on SOI. After development, the structure was transformed to silicon by reactive ion etching (RIE) using a CHF3/SF6 gas mixture. Then the wafer is split into a rectangular shape and also triangular shapes to obtain waveguides with different lengths. Thus, we can study the photoluminescence and transmission spectra with different propagation loss, and the incident angle between the fiber tip and the slab edge (triangular shape) would filter the noise from the slab, since femtosecond pulses in the slab and waveguide propagate with different directions. Single-layer highly n-doped graphene with centimeter scale was grown on copper foils by CVD with injection of NH_3 gas (XFNano Materials Tech.). PMMA is then spin-casted onto the graphene, and copper is removed by solution. It was transferred to water and then was transferred to the silicon waveguide surface, and finally the PMMA layer was dissolved.

Silicon ridge waveguides were fabricated from a 1.5 μm thick silicon on a 1.0 μm thick insulator wafer, in order to observe the weak pumped photoluminescence of graphene and demonstrate the Fabry−Perot interference effect from the silicon substrate. The width of the waveguides is 1.5 μm, and the etched thickness is 0.40 μm. After transfer of graphene, no photoluminescence could be detected by OSA 1 (Figure 3a, dark yellow dot−dashed line), since the electrical field on the graphene surface is very weak. We thus fabricated slot-like waveguides by depositing (Oerlikon Leybold Vacuum) 30 nm thick SiO_2 and 100 nm Si_3N_4 on top of the graphene to enhance the light intensity at the graphene layer.

The samples were placed on a 5-Axis NanoBlock Device Platform (Thorlab) under a stereomicroscope (ZEISS Stem 2000-C) and a microscope stand (ZEISS Axio ScopeA1). Our femtosecond laser has an output power of 20 mW (10 mW at

DOI: 10.1021/acsphotonics.5b00051
ACS Photonics 2015, 2, 797−804

the fiber tip), center wavelength of 1.57 μm, pulse width of 130 fs, and repetition rate of 100 MHz (Menlo Systems C-Fiber). The continuous laser source is a combination of a tunable laser (Agilent 8160A) and a standard fiber amplifier (Keopsys, KPS-STD-BT-C-33-SLM-PM). The laser was coupled to the sample by a single mode fiber with a tapered lens (Chuxing Ltd.) with a focal spot diameter of about 4 μm. The minimum coupling insertion loss is estimated to be 10 dB. The incident power was tuned by changing the coupling insertion loss between the fiber tip and the sample.

Light emission photos were captured by a CCD camera at the eyepiece of the microscope. Vertically emitted light from the microarea was collected by an objective lens on top of the sample surface and was focused to the fiber by a fiber collimator (Supporting Information S8). It was then coupled to an OSA with a cooled CCD array (Ideaoptics NOVA, at −20 °C). The received signal was divided by the spectral response of the CCD (Supporting Information S9). Transmitted light in the wafer plane was collected by an objective lens with NA = 0.67 and then was focused to a single-mode fiber and coupled to an OSA (Yokogawa AQ6370 and AQ6375). Raman measurements were performed with Bruker SENTERRA.

All the emission spectra have the same power scale units in this paper.

■ ASSOCIATED CONTENT

Supporting Information

The Supporting Information is available free of charge on the ACS Publications website at DOI: 10.1021/acsphotonics.5b00051.

■ AUTHOR INFORMATION

Corresponding Author

*E-mail: liukener@163.com.

Notes

The authors declare no competing financial interest.

■ ACKNOWLEDGMENTS

This work was supported by the National Natural Science Foundation of China (grant nos. 61205087, 61404174, 61177051). K.L. acknowledges Hua Hui Zhang for measurement preparation, Jing Hou, Ze Feng Wang, and Bin Zhang for the use of the AQ6375 infrared spectrometer, Xiao Feng Wang, Wei Chen, and Shu Fang Luo for SEM and Raman measurement, and Hong Jun Mao and Zong Fu Huang for help with the CCD setup. The authors thank Michel Orrit, Qingdong Zheng, Ting Yi Gu, Chee Wei Wong, Martin Mittendorff, Ermin Malic, Isabella Gierz, and Philip Hofmann for fruitful discussions.

■ REFERENCES

(1) Nair, R. R.; Blake, P.; Grigorenko, A. N.; Novoselov, K. S.; Booth, T. J.; Stauber, T.; Peres, N. M. R.; Geim, A. K. Fine structure constant defines visual transparency of graphene. *Science* **2008**, *320*, 1308.

(2) Novoselov, K. S.; Geim, A. K. S.; Morozov, S. V.; Jiang, D.; Katsnelson, M.; Grigorieva, I. I. V.; Dubonos, S. V.; Firsov, A. A. Two-dimensional gas of massless Dirac fermions in graphene. *Nature* **2005**, *438*, 197−200.

(3) Castro Neto, A. H.; Guinea, F.; Peres, N. M. R.; Novoselov, K. S.; Geim, A. K. The electronic properties of graphene. *Rev. Mod. Phys.* **2009**, *81*, 109−162.

(4) Das, S.; Adam, S.; Hwang, E. H.; Rossi, E. Electronic transport in two-dimensional graphene. *Rev. Mod. Phys.* **2011**, *83*, 407−470.

(5) Liu, M.; Yin, X.; Ulin-Avila, E.; Geng, B.; Zentgraf, T.; Ju, L.; Wang, F.; Zhang, X. Graphene-based broadband optical modulator. *Nature* **2011**, *474*, 64−67.

(6) Gan, X.; Shiue, R. J.; Gao, Y.; Meric, I.; Heinz, T. F.; Shepard, K.; Hone, J.; Assefa, S.; Englund, D. Chip-integrated ultrafast graphene photodetector with high responsivity. *Nat. Photonics* **2013**, *7*, 883−887.

(7) Wang, X.; Cheng, Z.; Xu, K.; Tsang, H. K.; Xu, J. B. High-responsivity graphene/silicon-heterostructure waveguide photodetectors. *Nat. Photonics* **2013**, *7*, 888−891.

(8) Pospischil, A.; Humer, M.; Furchi, M.; Bachmann, D.; Guider, R.; Fromherz, T.; Mueller, T. CMOS-compatible graphene photodetector covering all optical communication bands. *Nat. Photonics* **2013**, *7*, 892−896.

(9) Hendry, E.; Hale, P. J.; Moger, J.; Savchenko, A. K.; Mikhailov, S. A. Coherent nonlinear optical response of graphene. *Phys. Rev. Lett.* **2010**, *105*, 097401.

(10) Gu, T.; Petrone, N.; McMillan, J. F.; Zande, A.; Yu, M.; Lo, G. Q.; Kwong, D. L.; Hone, J.; Wong, C. W. Regenerative oscillation and four-wave mixing in graphene optoelectronics. *Nat. Photonics* **2012**, *6*, 554−559.

(11) Kumar, N.; Kumar, J.; Gerstenkorn, C.; Wang, R.; Chiu, H. Y.; Smirl, A. L.; Zhao, H. Third harmonic generation in graphene and few-layer graphite films. *Phys. Rev. B* **2013**, *87*, 121406(R).

(12) Hong, S. Y.; Dadap, J. I.; Petrone, N.; Yeh, P.; Hone, J.; Osgood, R. M., Jr. Optical third-harmonic generation in graphene. *Phys. Rev. X* **2013**, *3*, 021014.

(13) Koyama, T.; Ito, Y.; Yoshida, K.; Tsuji, M.; Ago, H.; Kishida, H.; Nakamura, A. Near-Infrared photoluminescence in the femtosecond time region in monolayer graphene on SiO_2. *ACS Nano* **2013**, *7*, 2335−2343.

(14) Säynätjoki, A.; Karvonen, L.; Riikonen, J.; Kim, W.; Mehravar, S.; Norwood, R. A.; Peyghambarian, N.; Lipsanen, H.; Kieu, K. Rapid large-area multiphoton microscopy for characterization of graphene. *ACS Nano* **2013**, *7*, 8441−8446.

(15) Liu, W. T.; Wu, S. W.; Schuck, P. J.; Salmeron, M.; Shen, Y. R.; Wang, F. Nonlinear broadband photoluminescence of graphene induced by femtosecond laser irradiation. *Phys. Rev. B* **2010**, *82*, 081408(R).

(16) Lui, C. H.; Mak, K. F.; Shan, J.; Heinz, T. F. Ultrafast photoluminescence from graphene. *Phys. Rev. Lett.* **2010**, *105*, 127404.

(17) Chen, C. F.; Park, C.-H.; Boudouris, B. W.; Horng, J.; Geng, B.; Girit, C.; Zettl, A.; Crommie, M. F.; Segalman, R. A.; Louie, S. G.; Wang, F. Controlling inelastic light scattering quantum pathways in graphene. *Nature* **2011**, *471*, 617−620.

(18) Mak, K. F.; Ju, L.; Wang, F. Optical spectroscopy of graphene: From the far infrared to the ultraviolet. *Solid State Commun.* **2012**, *152*, 1341−1349.

(19) Das, A.; Pisana, S.; Chakraborty, B.; Piscanec, S.; Saha, S. K.; Waghmare, U. V.; Novoselov, K. S.; Krishnamurthy, H. R.; Geim, A. K.; Ferrari, A. C.; Sood, A. K. Monitoring dopants by Raman scattering in an electrochemically top gated graphene transistor. *Nat. Nanotechnol.* **2008**, *3*, 210−215.

(20) Zheng, Q. D.; Zhu, H. M.; Chen, S. C.; Tang, C. Q.; Ma, E.; Chen, X. Y. Frequency-upconverted stimulated emission by simultaneous five-photon absorption. *Nat. Photonics* **2013**, *7*, 234−239.

(21) Brida, D.; Tomadin, A.; Manzoni, C.; Kim, Y. J.; Lombardo, A.; Milana, S.; Nair, R. R.; Novoselov, K. S.; Ferrari, A. C.; Cerullo, G.; Polini, M. Ultrafast collinear scattering and carrier multiplication in graphene. *Nat. Commun.* **2013**, *4*, 1987.

(22) Cho, C. H.; Aspetti, C. O.; Park, J.; Agarwal, R. Silicon coupled with plasmon nanocavities generates bright visible hot luminescence. *Nat. Photonics* **2013**, *7*, 285−289.

(23) Coldren, L. A.; Corzine, S. W. Optical Gain & Auger Recombination. In *Diode Lasers and Photonic Integrated Circuits*; J. Wiley and Sons: New York, 1995; pp 126−127 and 153−160.

(24) Ulstrup, S.; Bianchi, M.; Hatch, R.; Guan, D.; Baraldi, A.; Alfè, D.; Hornekær, L.; Hofmannn, Ph. High-temperature behavior of

DOI: 10.1021/acsphotonics.5b00051
ACS Photonics 2015, 2, 797−804

supported graphene: Electron-phonon coupling and substrate-induced doping. *Phys. Rev. B* **2012**, *86*, 161402R.
(25) Winzer, T.; Knorr, A.; Malic, E. Carrier multiplication in graphene. *Nano Lett.* **2010**, *10*, 4839−4843.
(26) Winzer, T.; Ciesielski, R.; Handloser, M.; Comin, A.; Hartschuh, A.; Malic, E. Microscopic view on the ultrafast photoluminescence from photoexcited graphene. *Nano Lett.* **2015**, *15*, 1141−1145.
(27) Gierz, I.; Petersen, J. C.; Mitrano, M.; Cacho, C.; Turcu, I. C.; Springate, E.; Stöhr, A.; Köhler, A.; Starke, U.; Cavalleri, A. Snapshots of non-equilibrium Dirac carrier distributions in graphene. *Nat. Mater.* **2013**, *12*, 1119.
(28) Mittendorff, M.; Wendler, F.; Malic, E.; Knorr, A.; Orlita, M.; Potemski, M.; Berger, C.; Heer, W. A.; Schneider, H.; Helm, M.; Winnerl, S. Carrier dynamics in Landau-quantized graphene featuring strong Auger scattering. *Nat. Phys.* **2015**, *11*, 75−81.
(29) Tielrooij, K. J.; Song, J. C.W.; Jensen, S. A.; Centeno, A.; Pesquera, A.; Elorza, A. Z.; Bonn, M.; Levitov, L. S.; Koppens, F. H. L. Photoexcitation cascade and multiple hot-carrier generation in graphene. *Nat. Phys.* **2013**, *9*, 248−252.
(30) Yan, J.; Zhang, Y.; Kim, P.; Pinczuk, A. Electric field effect tuning of electron-phonon coupling in graphene. *Phys. Rev. Lett.* **2007**, *98*, 166802.

DOI: 10.1021/acsphotonics.5b00051
ACS Photonics 2015, 2, 797−804